A Search for Solar Axions

with the MICROMEGAS Detector

in CAST

Vom Fachbereich Physik der

TECHNISCHEN UNIVERSITÄT DARMSTADT

zur Erlangung des Grades
eines Doktors der Naturwissenschaften
(Dr. rer. nat.)

genehmigte Dissertation von
Theopisti Dafni
aus Thessaloniki

Darmstadt 2005
D17

Referent: Prof. Dr. D. H. H. Hoffmann
Korreferent: Prof. Dr. P. Braun-Munzinger

Tag der Einreichung: 11.04.2005
Tag der Prüfung: 29.06.2005

Zusammenfassung

Die experimentelle Suche nach Axionen wird unter anderem durch das sogenannte CP-Problem der starken Wechselwirkung motiviert: die Theorie sagt eine Verletzung der CP-Symmetrie für die starke Wechselwirkung vorher, die bislang jedoch in keinem Experiment nachgewiesen werden konnte. Peccei und Quinn führten eine neue Symmetrie ein, um das Problem zu lösen: eine Symmetrie, die mit einem neuen, fast masselosen Boson, nämlich dem Axion, verknüpft ist. Das Axion ist sehr faszinierend, wenn man die Anzahl und Vielfalt der Anwendungen, die seine Existenz impliziert, betrachtet: neben der Tatsache, dass es eine elegante Lösung des CP-Problems liefert, ist es einer der zwei überlebenden Kandidaten für die "Dunkle Materie".

Kosmologie und Astrophysik geben bereits erste Einschränkungen der Eigenschaften der Axionen bezüglich ihrer Masse und ihrer Kopplung an Fermionen, Nukleonen und Photonen. Beachtet man alle diese Beschränkungen, so bleibt nur noch ein kleines Fenster im Massenbereich von μeV bis zu einigen eV offen, in dem Axionen zu erwarten sind. Mehrere Experimente nutzen den Primakoff- Effekt, um nach Axionen zu suchen. In diesem Prozess kann ein Axion in einem elektrischen oder magnetischen Feld aus einem Photon entstehen und umgekehrt besteht die Möglichkeit, dass ein Axion sich unter ähnlichen Bedingungen in ein Photon umwandelt.

Mehrere Methoden wurden entwickelt und in die Tat umgesetzt, um Axionen nachzuweisen. Das CAST-Experiment ist eines der Helioskope. Es benutzt einen fast 10 m langen Prototypmagneten, des im Aufbau befindlichen Large Hadron Collider (LHC) am Europäischen Kernforschungszentrum CERN in Genf. Dieser Magnet erreicht ein magnetisches Feld von 9 T. Er ist auf einem einem beweglichen Aufbau ähnlich einem astronomischen Teleskop montiert. Die Bewegung dieses Aufbaus erlaubt es, den Magneten fur etwa 100 Minuten während des Sonnenaufgangs auf die Sonne auszurichten. Für die gleiche Zeit kann die Sonne auch bei Sonnenuntergang beobachtet werden. Jede gegenuber dem Untergrund erhöhte Zahlrate, die nur während der Sonnenbeobachtung auftritt, wird als ein Signal der zu Photonen umgewandelten Axionen interpretiert.

Der Energiebereich der nachzuweisenden Photonen liegt zwischen 1 keV und etwa 10 keV und erfordert daher den Einsatz von Röntgendetektoren. Auf der dem Sonnenuntergang zugewandten Seite des Teleskops wird als Detektor eine Zeitprojektionskammer (Time Projektion Chamber, TPC) vewendet. Fur die Beobachtungszeit während des Sonnenaufgangs steht der in dieser Arbeit beschriebene Mikromegas-Detektor und ein Röntgenteleskop zur Verfügung. Das Röntgenteleskop, der Prototyp eines Röntgen-Spiegelteleskops der deutschen Röntgensatelliten-Mission ABRIXAS, das an einer der beiden Magnetöffnungen installiert ist, fokussiert die von den Axionen produzierten Photonen auf ein Charged Coupled Device (CCD).

An der anderen Magnetöffnung, die bei Sonnenaufgang Axionen beobachtet, befindet sich ein Micromegas-Detektor. Dabei handelt es sich um einen Gasdetektor der Mikrostreifen -Art mit sehr asymmetrischer Doppelstruktur. Zusammen mit der hohen Granularität (384 Streifen) hat der Detektor eine sehr gute Orts- und Energieauflösung. Ein weiterer interessanter Punkt für diese Anwendung ist die hohe erreichte Unterdrückung

des Untergrundes. Der CAST- Prototyp war der erste Micromegas-Detektor, bei dem eine zweidimensionale Auslese der Streifen realisiert wurde. Eine zusätzliche Auslese des Signals vom Gitter wurde ebenso benutzt und erlaubte es, mehr Informationen zu nutzen, um damit die Untergrundunterdrückung noch zu erhöhen.

Das Experiment schloss Ende des Jahres 2004 erfolgreich die erste Phase von CAST mit einer Laufzeit von zwei Jahren ab, ohne ein statistisch signifikantes Signal beobachtet zu haben. Diese Arbeit beschreibt die Analyse der Daten, die vom Micromegas-Detektor während dieser ersten Phase aufgenommen wurden. Für das erste Jahr (2003) führte diese Analyse fur den Micromegas-Detektor zu einer Obergrenze der Kopplungskonstante für eine Umwandlung von Axionen in Photonen von

$$g_{a\gamma} \leq 1.5 \times 10^{-10}\,\mathrm{GeV}^{-1}$$

in einem statistischen Vertrauensintervall (Confidence Level, C.L.) von 95% bei Axionmassen bis zu 0.02 eV. Der erste vollständige Blick auf die Daten des zweiten Jahres fuhrt zu einer Obergrenze von

$$g_{a\gamma} \leq 1.22 \times 10^{-10}\,\mathrm{GeV}^{-1}$$

bei 95% C.L. fur denselben Massenbereich.

Durch Kombination der Ergebnisse aller Detektoren fur das Jahr 2003 hat das Experiment die Axion-Photon-Kopplungskonstante um einen Faktor 5 -verglichen mit den bisherigen Experimenten- verbessert auf

$$g_{a\gamma} \leq 1.16 \times 10^{-10}\,\mathrm{GeV}^{-1}$$

für $m_a \leq 0.02\,\mathrm{eV}$.

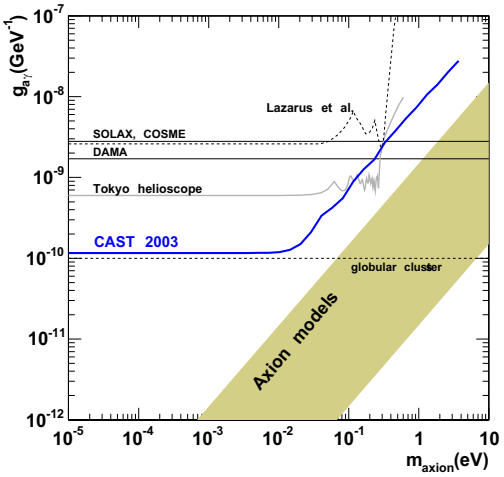

Figure 1: Ausschlussgrenze bei 95% C.L. aus den CAST-Daten für 2003. Verglichen mit anderen Experimenten gibt CAST die niedrigste Obergrenze. (Der schattierte Bereich steht für die typischen theoretischen Modelle).

Abstract

The CAST Experiment completed its first phase in the end of 2004, after having run successfully for two years. The results of the data analysis of the Micromegas detector at CAST for 2003 and a first result of 2004 are presented here. This experiment has a sensitivity of almost a factor 100 better compared with previous searches.

The coupling constant of axions of mass up to 0.02 eV to photons has been restricted with a 95% Confidence Level to

$$g_{a\gamma} \leq 1.50 \times 10^{-10}\,\mathrm{GeV}^{-1}$$

for the 2003 Micromegas detector [and $g_{a\gamma} \leq 1.16 \times 10^{-10}\,\mathrm{GeV}^{-1}$ after combining the result of all the detectors of the experiment]. The preliminary limit acquired for the 2004 data is more strict, at

$$g_{a\gamma} \leq 1.21 \times 10^{-10}\,\mathrm{GeV}^{-1}$$

concerning the Micromegas detector.

Contents

Chapter 1

Introduction

The discussion on axions has its roots in the strong-CP problem: theory predicts a CP violation from the strong interactions, which Nature has never exhibited in any experiment. Peccei and Quinn introduced a new symmetry to solve the problem, a symmetry which hid a new, almost massless boson, the axion. The axion is rather fascinating if one is to judge by the number and variety of applications its existence has suggested:

- rather aged as one of the two survivor candidates of the "Dark Matter" that should be around us, accounting for the 25% of the density of the Universe, or even
- a baby having just been born in the core of a star, like the Sun.

Cosmology and astrophysics have already given the first constraints on the properties of the axions (regarding their mass and couplings to fermions, nucleons and photons). Gathering all these bounds, only a small window in the mass range of μeV to some tens of meV "survives" to allow for axions to sit in. Several experiments have been looking for axions taking advantage of the Primakoff effect. According to this process, an axion can be born from a photon in the presence of an electric or magnetic field, and vice versa, the axion has a chance to convert to a photon under similar conditions.

Several techniques have been invented and put into act for the detection of axions. Tunable microwave cavities permeated with magnetic field are waiting for relic axions lingering in our galactic halo to be converted into photons; laser beams are sent through magnetic fields or on walls, in the hope of producing axions; conversion of axions in crystals has been exploited through a Primakoff-Bragg effect; magnets are pointing at the Sun, offering the axion tempting reasons to leave the signature of its existence via a photon.

The CAST experiment is one of these helioscopes. It uses a nearly 10 m long Large Hadron Collider (LHC) decommissioned magnet that can reach a magnetic field of 9 T, which sits on a movable platform. The movement of the platform allows the magnet to be aligned with the Sun for approximately 100 min during sunset and just as much during sunrise. Any excess over the background which appears only during tracking times, will be a signal of axions-converted-to-photons.

If an axion is converted during the tracking, X-ray detectors are needed to detect the photon. Should it come during the sunset, a Time Projection Chamber (TPC), robust and with well known behaviour, will recover it. If it comes during sunrise, it would have to chose between the X-ray focusing system and MICROMEGAS. The prototype X-ray mirror telescope of the German X-ray satellite mission ABRIXAS, attached to one of the bores of the magnet, will focus the photons produced by axions onto a small-area Charged Couple Device (CCD), improving the signal-to-noise ratio by a factor of approximately 100.

The other bore, looking at sunrise axions, is covered by a Micromegas. It is a very asymmetric double structure of the micro-strip generation of gaseous detectors. In combination with high granularity (394 strips) the detector shows very good space and energy resolution. What is also very interesting for this application is the high background rejection achieved. The CAST prototype was the first one in which the 2-dimensional readout of the strips was implemented. An additional reading of the signal of the mesh, has been used as well, allowing to use more information in order to increase background rejection.

The experiment successfully concluded two years of running CAST Phase I at the end of 2004, without having observed any signal. This work describes the commissioning, operation analysis and first results of the Micromegas detector in the CAST experiment. A short introduction on how the axion came to exist, the properties it can hold and how they have to be limited according to cosmological, astrophysical and experimental observations are given in the beginning. A detailed description of the CAST experiment comes next. The properties and performance of the Micromegas detector in detail follow, to reach the chapter with the results of the analysis of the 2003 data. The first result for 2004 data is presented in the previous-to-last chapter. The final chapter contains conclusive remarks, accompanied by some words for the future.

Chapter 2

Axions

A brief introduction on how the axion came to be sought after by many experiments, is given in this chapter: what the axion is, its properties and the limits set on them by astrophysics, cosmology and experiments so far.

2.1 The strong-CP Problem and its solution

A problem

A spontaneously broken symmetry is a symmetry that is valid for the Lagrangian but not for the vacuum (ground) state of the system. As a general theorem, whenever a continuous global symmetry is spontaneously broken, the spectrum will have a massless, spin-zero boson (Nambu-Goldstone boson). If the symmetry is not exact though, the associated particle has a small mass, and is called a "pseudo-Goldstone boson".

When examining the Quantum Chromodynamics (QCD) Lagrangian, given (for f flavour of quarks) by

$$\mathcal{L}_{\mathrm{QCD}} = -\sum_f \bar{q}\left(\gamma^\mu \frac{1}{i} D_\mu + m_f\right) q_f - \frac{1}{4} G_a^{\mu\nu} \widetilde{G}_{a\mu\nu} \quad , \tag{2.1}$$

there is a global symmetry in the limit for $m_f \to 0$, denoted as $G = U(f)_R \times U(f)_L$. Regarding the u and d quarks – the masses are relatively small and in the limit they are set to zero – the theory shows a symmetry $U(2)_L \times U(2)_R$. The vectorial part of this symmetry $U(2)_{L+R}$ (and its subgroup $U(1)_V = U(1)_{L+R}$) is an exact symmetry. On the

other hand, the axial part ($U(2)_A = U(2)_{L-R}$) is not preserved by the QCD vacuum, and –following the above mentioned theorem– four Goldstone bosons are expected. Three of them (corresponding to the $SU(2)_A$ breaking) have been noticed; the pion triplet π^- , π^0 , π^+. However the expected fourth boson, related to the $U(1)_A$ breaking, does not exist. This is the $U(1)_A$ problem[1,2].

It turns out [3, 4], that the answer to the problem lies between the fact that $U(1)_A$ has a chiral (otherwise called axial or triangle or Adler-Bell-Jackiw) anomaly and that the ground state (vacuum) of QCD is non-trivial. In fact, the QCD vacuum has infinitely degenerate vacua, topologically different. The transition from one vacuum class to another is classically forbidden, yet due to quantum tunneling, this transition has a non-zero amplitude. Instantons describe a solution, localized in space and time, in which a vacuum of class $n-1$ evolves into another vacuum, of class n. This integer, n, is the topological winding number, labeling each of the vacua. The superposition of the various vacua is called the Θ-vacuum, and can be written as a function of the parameter Θ :

$$|\Theta >= \sum_n e^{-in\Theta} |n > \quad . \tag{2.2}$$

At the same time, considering the effect of the chiral anomaly of the $U(1)_A$ symmetry, an extra term is added to the Lagrangian, changing it to

$$\mathcal{L}^{\text{eff}}_{\text{QCD}} = \mathcal{L}_{\text{QCD}} + \Theta \frac{g^2}{32\pi} G^{\mu\nu}_a \widetilde{G}_{a\mu\nu} \quad , \tag{2.3}$$

(where Θ is the above mentioned Θ parameter) or, including the electroweak interactions to

$$\mathcal{L}^{\text{eff}}_{\text{SM}} = \mathcal{L}_{\text{SM}} + \bar{\Theta} \frac{g^2}{32\pi} G^{\mu\nu}_a \widetilde{G}_{a\mu\nu} \quad . \tag{2.4}$$

where $\mathcal{L}_{\text{SM}}$ is the Standard Model Lagrangian. Here Θ is substituted by an *effective* $\bar{\Theta}$ parameter

$$\bar{\Theta} = \Theta + \text{Arg}(\det M) \quad , \tag{2.5}$$

which takes into account both QCD and electroweak information: quarks acquire their effective masses through the breakdown of the electroweak symmetry, and M is the quark mass matrix.

Because of the non-trivial properties of the Θ-vacuum, and the axial anomaly of $U(1)_A$ it was shown [3, 4] that $U(1)_A$ is not really a quantum symmetry of QCD, and therefore no Nambu-Goldstone boson is expected associated with this symmetry; η does not need to be lighter than it is.

[1]Put in a different way, the only other possible particle, the η meson, although it has the right quantum numbers ($J^P = 0^-$) is remarkably heavy ($m_\eta = 958\,\text{MeV}$ while $m_\pi = 135\,\text{MeV}$). So another expression of the $U(1)_A$ problem would be "why is η so heavy?".

[2]For a complete discussion on the subject, one should refer to [1, 2].

Another problem

As much as it helped resolve the $U(1)_A$ problem, the implementation of $\bar{\Theta}$ induces another one: its presence implies violation of the CP invariance in QCD, which has never been observed.

Electric dipole moments are the most interesting parameters connected to CP violation. The electric dipole moment of the neutron has a strong experimental bound at $|d_n| \leq 12 \times 10^{-26}$ e cm. However, a simple dimensional analysis of this quantity yields a value for $d_n \sim 10^{-16}$ $\bar{\Theta}$ e cm. This automatically constrains $\bar{\Theta}$ to $\bar{\Theta} \lesssim 10^{-9}$. The smallness of $\bar{\Theta}$ implies an extreme fine-tunning of Θ to the value of $\mathrm{Arg}\det M$, for these contributions to cancel to the order of $\bar{\Theta}$. The question of the smallness of $\bar{\Theta}$, is known as "the Strong-CP problem".

A solution to the strong-CP problem

An elegant answer to this problem was supplied by Peccei and Quinn [5, 6]: the extension of the Standard Model with an additional, spontaneously broken, global chiral $U(1)$ symmetry (the $U(1)_{PQ}$), such that changes to $\bar{\Theta}$ are equivalent to changes in the definitions of the various fields of $\mathcal{L}^{\mathrm{eff}}_{\mathrm{SM}}$. In that case, any change in $\bar{\Theta}$ has no physical consequence and is equivalent to a $\bar{\Theta} = 0$, leaving no strong-CP violation. From the breaking of the symmetry a pseudo Nambu-Goldstone boson emerges, the *axion*[3] [7, 8].

2.2 Introducing the axion

If f_a is the scale of the spontaneous breakdown of $U(1)_{PQ}$, the axion field $a(x)$ will transform under the new symmetry as

$$a(x) \overset{PQ}{\rightarrow} a(x) + \alpha f_a \ . \tag{2.6}$$

Because of the chiral anomaly of this symmetry, the axion will couple to gluons, resulting in the appearance of an extra term (linearly depending on $a(x)$) in the Lagrangian

$$\mathcal{L}_{\mathrm{axion}} = \frac{a(x)}{f_a}\xi\frac{g^2}{32\pi^2}G^{\mu\nu}_a\widetilde{G}_{a\mu\nu} - \frac{1}{2}\partial_\mu a\partial^\mu a + \mathcal{L}(\partial_\mu a, \psi) \tag{2.7}$$

for ξ a model depending parameter, $\frac{1}{2}\partial_\mu a\partial^\mu a$ the kinetic energy of the axion field and $\mathcal{L}(\partial_\mu a, \psi)$ stands for the possible interaction of the axion field with a fermion ψ. The first term of this equation gives the axion field an effective potential, allowing it to relax not in all values of vacuum, but only in those that minimize this potential

$$\left\langle \frac{\partial V_{\mathrm{eff}}}{\partial a} \right\rangle = 0 \Longrightarrow < a > = -\frac{f_a}{\xi}\bar{\Theta} \ . \tag{2.8}$$

[3] The axion was named after a laundry detergent, "since they clean up a problem with an axial current" [9].

The strong-CP problem is solved: the physical axion field

$$a_{\text{phys}} = a - \ < a > \tag{2.9}$$

absorbs the $\bar{\Theta}$ dependent term and no violation occurs.

All is left to do is experimentally verify that the axion exists.

2.3 Axion Properties

The axion properties depend on the axion decay constant, f_a, the breaking scale of the PQ symmetry. The most significant feature of the axion couplings g_{aii} is that they are proportional to $1/f_a$ or equivalently, proportional to m_a.

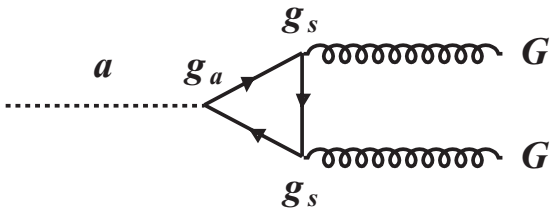

Figure 2.1: The triangle loop of the interactions of axions to gluons, where g_s is the strong coupling constant and g_a the axion-fermion Yukawa coupling.

2.3.1 Coupling to Gluons

The introduction of the physical axion field (equation (2.9)) in the Lagrangian, cancels the $\bar{\Theta}\, G_a^{\mu\nu}\widetilde{G}^a_{\mu\nu}$ term, but leaves another part, $a_{\text{phys}}G_a^{\mu\nu}\widetilde{G}^a_{\mu\nu}$, the axion-gluon interaction (figure 2.1).

The coupling to gluons as a result of the chiral anomaly of the $U(1)_{PQ}$ symmetry,

$$\mathcal{L}_{aG} = \frac{\alpha_s}{8\pi f_a} G_a^{\mu\nu}\widetilde{G}_{a\mu\nu}\, a \tag{2.10}$$

is a direct outcome of any axion model, classifying it as the most generic property of the axions.

Mass

The mixing of the axion with gluons implies mixing with pions, and the mass the axion obtains can be extracted from :

$$m_a^2 = \frac{f_\pi^2 m_\pi^2}{f_a^2}\frac{z}{(1+z+w)(1+z)} \simeq 0.60\,\text{eV}\frac{10^7\,\text{GeV}}{f_a} \tag{2.11}$$

where $f_\pi \simeq 93\,\mathrm{MeV}$ and $m_\pi = 135\,\mathrm{MeV}$ are the decay constant and mass of the pion, respectively, and

$$\begin{aligned} z &\equiv m_u/m_d \simeq 0.55 \pm 0.1 \\ w &\equiv m_u/m_s = 0.029 \pm 0.003 \end{aligned} \tag{2.12}$$

the quark mass ratios [10]. z is a quantity largely discussed. The value itself and its uncertainty vary significantly among calculations, for example from [11] one acquires $z \simeq 0.553 \pm 0.043$ while the Particle Data Group [12] gives a value of $0.3 \lesssim z \lesssim 0.7$.

Coupling to photons

The coupling of the axions to photons arises as a result of two contributions:

- Inevitably, the electromagnetic anomaly (the mixing with the neutral pions) generates coupling of the axions to photons as well as nucleons.
- In analogy to the coupling to gluons, if the fermions carrying PQ charges carry electric charges as well, they will couple (through a Yukawa coupling) the axion to two photons, via a triangle loop.

The two parts are shown schematically in figure 2.2.

The interaction will be according to

$$\mathcal{L}_{a\gamma} = -\frac{g_{a\gamma}}{4} F_a^{\mu\nu} \widetilde{F}_{a\mu\nu} = g_{a\gamma} \vec{E}\vec{B}\, a \tag{2.13}$$

where

$$g_{a\gamma} = \frac{\alpha}{2\pi f_a} \left(\frac{E}{N} - \frac{2(4+z+w)}{3(1+z+w)} \right) \quad . \tag{2.14}$$

for $F_a^{\mu\nu}$ the electromagnetic field strength tensor, $\widetilde{F}_{a\mu\nu}$ its dual, α the fine structure constant and $g_{a\gamma}$ the coupling constant. z and w are as defined above, equation (2.11). Introduced in equation (2.14), it becomes

$$g_{a\gamma} = \frac{\alpha}{2\pi f_a} \left(\frac{E}{N} - 1.93 \pm 0.08 \right) \quad . \tag{2.15}$$

The coupling constant includes a factor E/N, the ratio of the two anomaly coefficients, E the electromagnetic anomaly and N the color anomaly. If Q_j are the electric charges of the PQ fermions and X_j their PQ charge, E, N are defined as follows:

$$E \equiv 2 \sum_j X_j Q_j^2 D_j \quad N \equiv \sum_j X_j \quad , \tag{2.16}$$

were $D_j = 1$ for color singlets (charged leptons) and $D_j = 3$ for color triplets (quarks). Different models present different couplings to photons, because the values of these numbers are different for each one.

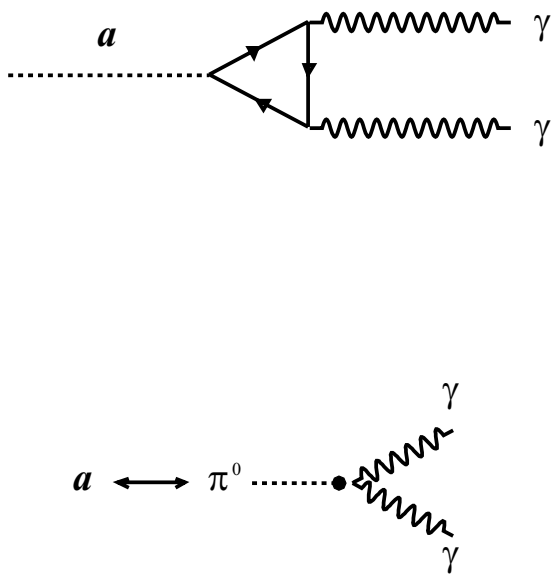

Figure 2.2: The two contributions to the axion-photon coupling: one from the coupling to fermions that carry PQ charge (i), and the second from the axion-pion mixing (ii).

Coupling to fermions

The coupling of axions with fermions is the main one distinguishing several models. Electrons and quarks would show Yukawa couplings to axions, if they (electrons and quarks) carry PQ charge. Because free quarks do not exist, the effective coupling of axions to nucleons can be studied. The tree-level interaction between axions and fermions, in a general form can be represented by

$$\mathcal{L}_{af} = \frac{g_{af}}{2m_f}\bar{\Psi}_f\gamma^\mu\gamma_5\Psi_f\partial_\mu a \quad . \tag{2.17}$$

f denotes the type of fermion (electron, nucleon) and

$$g_{af} = \frac{C_f\, m_f}{f_a} \tag{2.18}$$

the equivalent Yukawa coupling if m_f is the fermion mass. C_f stands for the effective PQ charge, a model-dependent quantity.

Tree-level coupling to electrons

Depending on the model, electrons may carry PQ charge, and therefore will interact as equation (2.17) describes. Following equation (2.18) in this case,

$$g_{ae}^{\text{tree}} = \frac{C_e\, m_e}{f_a} = C_e 0.85 \times 10^{-10} m_a \ . \tag{2.19}$$

Here $C_e = X'_e/N$, for X'_e the "effective" PQ charge of the electron.

Radiatively induced coupling to electrons

There are models for which the shifted charge $X'_e = 0$. For reasons of completeness, one should mention that even in that case, there exists an axion-to-electron coupling effectively, connected to a loop correction due to the interaction of axions with photons, with the form [13]:

$$g_{ae}^{\text{loop}} = \frac{3\alpha^2}{4\pi^2}\frac{m_e}{f_a}\left[\frac{E}{N}\ln\left(\frac{f_a}{m_e}\right) - \frac{2(4+z+w)}{3(1+z+w)}\ln\left(\frac{\Lambda_{\text{QCD}}}{m_e}\right)\right] \ . \tag{2.20}$$

where Λ_{QCD} is the QCD scale.

One can see that this loop correction is much weaker than the tree-level.

Coupling to nucleons

The coupling of axions to nucleons consists of two compounds, one derived from the tree-level coupling of axions to up and down quarks, and another emerging from the axion-pion mixing. Similarly to electrons, the coupling can be described by equation (2.18), giving

$$g_{aN} = \frac{C_N m_N}{f_a} \tag{2.21}$$

for the effective PQ charge of the nucleon C_N. Because of the two different parts of the interaction, C_N is a combination of the quarks' masses, and reads for protons and neutrons respectively:

$$\begin{aligned} C_p &= (C_u - \eta)\Delta u + (C_d - \eta z)\Delta d + (C_s - \eta w)\Delta s \\ C_n &= (C_u - \eta)\Delta d + (C_d - \eta z)\Delta u + (C_d - \eta w)\Delta s \ , \end{aligned} \tag{2.22}$$

with the forementioned (equation (2.11)) definitions of z, w and for $\eta \equiv 1/(1+z+w)$. Δu is the fraction of the nucleon's spin carried by the u quark, and the rest respectively. Substituting [14]

$$\begin{aligned} \Delta u &= +0.80 \pm 0.04 \pm 0.04 \\ \Delta d &= -0.46 \pm 0.04 \pm 0.04 \\ \Delta s &= -0.12 \pm 0.04 \pm 0.04 \end{aligned} \tag{2.23}$$

(statistical and systematic errors shown) in equation (2.22) and subsequently to equation (2.21), the axion-to-nucleon coupling constant is calculated.

2.4 Axion Models

Equation (2.11) exhibits the clear dependence of the axion's mass on the decay constant f_a. Different values of f_a classify axions in different categories: the larger the scale, the more weakly coupled and lighter the axion.

2.4.1 The visible axions

A very simple assumption (in fact the one made originally by Peccei and Quinn [5, 6]), would be that the decay constant is of the same order as the electroweak scale, so $f_a \simeq 250\,\text{GeV}$. This would be translated to an axion with a mass of about 100 keV. However, several experiments have excluded the existence of such *'visible'* axions rather soon: axions of that mass would be expected in the process

$$K^+ \to \pi^+ a \ .$$

A strong bound was set by the non observation of this process in KEK [15], for the branching ratio

$$BR(K^+ \to \pi^+ \text{ Nothing}) \leq 3.8 \times 10^{-8} \ ,$$

where "Nothing" is interpreted as a long lived axion which escapes detection, the strongest evidence against the visible axions.

2.4.2 The invisible axions

At the other end, if the scale f_a is much larger than f_{weak}, the coupling of the axion becomes weaker so much that it can have eluded all preliminary searches; it would be *'invisible'*. These models introduce a complex scalar field ϕ with a very large vacuum expectation value $< \phi >= f_{PQ}/\sqrt{2} \gg f_{\text{weak}}$. This field does not participate in the electroweak interactions. Two groups of models for the invisible axions have been considered: the KSVZ and DFSZ. Both groups are successful in their goal, to solve the strong-CP problem, however they conclude in different couplings of the axion.

The KSVZ axion

The Kim-Shifman-Vainshtein-Zakharov model [16] for axions suggests the existence of new, heavy quarks that carry Peccei-Quinn charge, while the usual leptons and quarks do not. The last statement puts $C_e = 0$ forbidding the KSVZ axion to couple to electrons in the tree level, and for this reason is known as the "hadronic" axion. Still, there is a very weak coupling to electrons for this type of axions as well, the radiatively induced one, discussed above.

Although normal quarks in this model do not feel the PQ symmetry (meaning $C_u = C_d = C_s = 0$), axions do couple with nucleons, according to equation (2.21). The coupling constants to nucleons are determined for the following values of the PQ-charge parameters (equations (2.22)):

$$\begin{aligned} C_p &= -0.34 \\ C_n &= 0.01 \ , \end{aligned} \tag{2.24}$$

leaving room for the Yukawa couplings of axions to protons and neutrons respectively

$$\begin{aligned} g_{ap} &= \frac{C_p m_p}{f_a} = -5.32 \times 10^{-8} m_a \\ g_{an} &= \frac{C_n m_n}{f_a} = 1.57 \times 10^{-9} m_a \ . \end{aligned} \tag{2.25}$$

Turning to the coupling to photons, equation (2.15) shows the dependence on the ratio E/N. Different models, within the KSVZ frame, give different values for this ratio. There can be models with $E/N \simeq 2$ [17], that suppress the photon coupling. In that case, the dominant contribution is from the coupling of axions to nucleons.

The DFSZ axion

In contrast to the previous model, in the Dine-Fischler-Srednicki-Zhitnitskiĭ model [18] normal quarks and leptons do feel the PQ symmetry (carry PQ charge). The ordinary Higgs field is substituted by two new ones, having vacuum expectation values f_1, f_2 respectively. In any Grand Unified Theory (GUT) for a given family of quarks and fermions, the ratio E/N equals to $8/3$, making

$$g_{a\gamma}^{\mathrm{DFSZ}} = 0.75 \frac{\alpha}{2\pi f_a} \ . \tag{2.26}$$

for the coupling to photons.

Since this ratio is given, the free parameters in this type of axions are two: the scale f_a^{DFSZ}, and the ratio $x = f_1/f_2$. In fact, the PQ-charge of the quarks and leptons are functions[4] of x (or rather β, defined as $\cos^2\beta = x^2(x^2+1)$) and hence the coupling constants to fermions are as well. The effective PQ charges for the fermions for this model, for N_f number of families, are as follows:

$$\begin{aligned} C_e = C_s = C_d &= \frac{\cos^2\beta}{N_f} \\ C_u + C_d &= \frac{1}{N_f} \\ C_u - C_d &= -\frac{\cos^2\beta}{N_f} \ , \end{aligned} \tag{2.27}$$

[4]Following the notation in [14]

leading to

$$\begin{aligned} C_e = C_s = C_d &= \frac{\cos^2\beta}{N_f} \\ C_u &= \frac{\sin^2\beta}{N_f} \ . \end{aligned} \tag{2.28}$$

Accepting that $N_f = 3$, equations (2.22) conclude to

$$\begin{aligned} C_p &= -0.08 - 0.46\cos^2\beta \\ C_n &= -0.14 + 0.38\cos^2\beta \ . \end{aligned} \tag{2.29}$$

2.5 Limits on axion properties from Cosmology and Astrophysics

Cosmological constraints

In order to derive information on the axion coupling and mass, one can deduct what the evolution of the axion expectation value would be through the Universe's life[5]. In the early Universe, this value is zero ($\bar{\Theta} = 0$ conventionally), but as soon as the Universe cools down to a temperature of the same range as the Peccei-Quinn scale, the expectation value of the axion field takes some chance value Θ_i (initial "misalignment"). Cooling down to a temperature where the axion mass becomes comparable to the Universe expansion rate, the axion field starts to settle down and oscillate around its final dynamical value ($\bar{\Theta} = 0$). The energy density accumulated in this oscillations of the axion field, should not exceed the energy density which closes the Universe. Expressing the abundance of axions $\Omega_a h^2$ as a function of the misalignment angle

$$\Omega_a h^2 \simeq 1.9 \times 3^{\pm 1} \left(\frac{1\mu\,\mathrm{eV}}{m_a}\right)^{1.175} \Theta_i^2 f(\Theta_i) \tag{2.30}$$

where h^2 is the Hubble constant (in units of $100\,\mathrm{kms}^{-1}\mathrm{Mpc}^{-1}$), and any anharmonic corrections on the axion potential are incorporated in $f(\Theta_i)$. The Wilkinson Microwave Anisotropy Probe (WMAP) data gives a matter density of $\Omega_m h^2 = 0.135^{+0.008}_{-0.008}$ [23]. Assuming an abundance for the axions of the same order, and they would dominate the Cold Dark Matter of the Universe, if m_a was of the order of μeV. The breakdown of a continuous $U(1)$ symmetry generally allows a one-dimensional topological solution with a linear mass density, determined by the parameter u^2 of the symmetry breaking. In that case, strings form in the cosmic evolution.

[5] A further discussion on the cosmological and astrophysical constraints can be found in the reports and reviews of Kim [19], Turner [20] and Raffelt [21], as well as in the PDG [12].

The axion models have spontaneously broken $U(1)_{PQ}$ symmetries, therefore in the case that inflation did not occur at all or if it did, it occurred after the spontaneous breaking of this symmetry, cosmic axion strings would appear. The axion production through this mechanism depends on the average energy of an axion produced by string dissipation at time t. There is a controversy over the matter between Battye and Shellard [24] and Sikivie *et al.* [25, 26]: according to Battye and Shellard, following the notion that the energy of the axionic strings turns into axions, the mass density that thus produced axions would contribute would be

$$\Omega_{\text{string}} h^2 \simeq \frac{m_a \text{eV}^{-1.175}}{10^{-3}} \quad , \tag{2.31}$$

restricting the axion mass to

$$m_a \gtrsim 10^{-4}\,\text{eV}\,.$$

On the other hand, Sikivie *et al.*'s reasoning, that the string radiation goes more into kinetic axion energy, these axions wouldn't increase the density of relic axions significantly more than the "misalignment mechanism" given by equation (2.30). If they are correct, the axion mass should be

$$m_a \gtrsim 10^{-6}\,\text{eV}\,.$$

Finally, it has been noted that axions with a mass above 0.1 eV, called "multi-eV" axions [40], have lifetimes which are long enough to support that not all relic axions have decayed until now, yet short enough for quite some of them to be decaying at present. The produced photons must be monoenergetic and will provide line radiation that could be detected.

This discussion covers the case where axions were never in thermal equilibrium, meaning that the scale f_a is quite large ($f_a \geq 10^8\,\text{GeV}$) and axions are weakly interacting. In the case that they interacted strongly and the scale were small enough ($f_a \leq 10^8\,\text{GeV}$), axions would have been in good thermal contact with the universal plasma and there should exist a background sea of invisible axions. Astrophysical arguments disfavour this possibility.

Constraints introduced by Astrophysics

The existence of the axion, assumed to be produced in the stellar plasma, would mean a novel energy-loss mechanism for stars. A possible axion emission would modify stellar evolution in a way that it would directly affect an observable, like the lifetime of the star; if axions carry away energy from the star, the star will increase its burning fuel in the center, in order to compensate the loss, speeding up its evolution and therefore shortening its lifetime.

Globular cluster stars have nearly the same age, but differ mainly in their mass. Red giants and Horizontal Branch (HB) stars provide restrictive bounds on the couplings of axions to electrons (DFSZ axions) and photons. Arguments as the one mentioned for the stars' lifetimes bind the axion-to-photon coupling with

$$g_{a\gamma} \lesssim 1 \times 10^{-10}\,\text{GeV}^{-1} \quad , \tag{2.32}$$

and their mass

$$m_a \lesssim 0.3 \left(\frac{E}{N} - 1.93 \pm 0.08 \right) \quad . \tag{2.33}$$

A bremsstrahlung process

$$e^- + (A, Z) \rightarrow e^- + (A, Z) + a$$

would delay the helium flash in the red-giants' core, allowing the core to accumulate more mass until helium ignition. Observations restrict (for the DFSZ axions)

$$g_{ae}^{\mathrm{DFSZ}} \lesssim 2.5 \times 10^{-13}\,\mathrm{GeV}^{-1} \quad . \tag{2.34}$$

The most restrictive limits come from observations of the newly born SN 1987A, when referring to axions produced via nucleon-nucleon-axion bremsstrahlung

$$N + N \rightarrow N + N + a$$

in its core. In that case, the energy-loss of the supernova would result in (i) shortening the length of the observed neutrino burst, (ii) a possible increase in the number of counts in the neutrino detectors or (iii) axions would radiatively decay.

Taking into account the observations of Kamiokande II and the Irvine-Michigan-Brookhaven (IBM) detectors, the coupling of axions to nucleons in the range [14]

$$3 \times 10^{-10}\,\mathrm{GeV}^{-1} \lesssim g_{aN} \lesssim 3 \times 10^{-7}\,\mathrm{GeV}^{-1} \quad , \tag{2.35}$$

is excluded, deriving an exclusion range for the mass:

$$0.01\,\mathrm{eV} \quad \lesssim \quad m_a^{\mathrm{KSVZ}} \lesssim 10\,\mathrm{eV} \tag{2.36}$$

Heavy hadronic axions could induce nuclear excitations that could deexcite via detectable γ-rays. This would mean an increase in the number of observed events in the water- Čerenkov detectors, hence another mass range [27]

$$20\,\mathrm{eV} \quad \lesssim \quad m_a^{\mathrm{KSVZ}} \lesssim 20\,\mathrm{keV} \tag{2.37}$$

is excluded.

All these observations and calculations leave only a small window in the mass range for hadronic axions to exist, axions with mass in the range μeV to decades of meV . Figure 2.3 summarizes these constraints and shows this window. It should be stressed at this point, though, that both the astrophysical and the cosmological bounds are rather uncertain, and have not stopped researchers from looking for axions exploring even the "forbidden" regions.

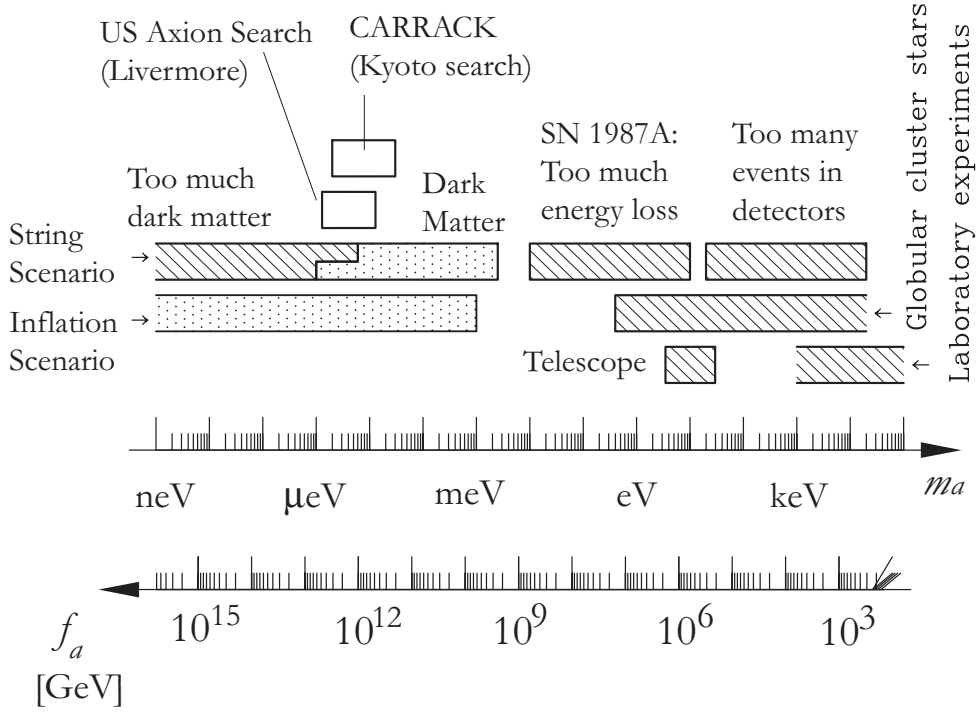

Figure 2.3: A summary on the astrophysical and cosmological regions of exclusion for the axion mass (or, equivalently for the Peccei-Quinn scale f_a). The bars with open ends represent a rough estimate, for example the one for the globular cluster stars, given here for the DFSZ model. The SN 1987A limit is for the KSVZ one, but covers approximately the DFSZ model as well. The regions with the dots (labeled 'inflation scenario' and 'dark matter') are the regions where the axion could be the dark matter and the black ones the sensitivity of the search experiments for galactic dark-matter axions.(Taken from [14])

2.6 Axion Detection

Sikivie in 1983 [28], was the first to show that the invisible axions were not really such, proposing several experiments, all based in the axion-to-photon conversion, the Primakoff effect. Since then, several experimental techniques have been invented for axion searches, and many experiments have come up with results constraining $g_{a\gamma}$:

- **Microwave cavity experiments:** Looking for galactic halo axions, electromagnetic cavities with strong static magnetic field can be helpful (details can be found in a recent review [29] and the references therein). Fine-tuning the frequency of the cavity so that it matches their mass m_a, the axions will convert resonantly to photons, according to the coupling constant (equation (2.14)). Early experiments (Rochester-Brookhaven-Fermilab [30, 31], the University of Florida Experiment [32]) were able to scan quite a range of frequencies, and precluded a range in the mass axis of

  $$4.5\,\mu\text{eV} < m_a < 16.3\,\mu\text{eV}\,.$$

  Second generation experiments, use –or are going to use– essentially the same techniques, but with better sensitivity; the ADMX experiment [33, 34] is continuously taking data and have already excluded the mass range

  $$1.9\,\mu\text{eV} < m_a < 3.3\,\mu\text{eV}\,.$$

  The experiment will enhance its sensitivity, hopefully toward a definitive axion search, implementing a technology based on Superconducting Quantum Interference Devices (dc SQUID) [35]. A large-scale detector for axion search has been built in Japan; CARRACK2 (Cosmic Axion Research using Rydberg Atoms in a resonant cavity in Kyoto), is being commissioned, using a Rydberg atom single-quantum detector [36, 37]. This large-scale detector will cover the region of

  $$2\,\mu\text{eV} \lesssim m_a \lesssim 30\,\mu\text{eV}\,.$$

  Already CARRACK I [38] (the prototype) has searched for axions at the $10\,\mu$eV region, and the results are being evaluate.

- **Optical and RadioTelescope searches:** Searches have also been performed for the thermally produced axions, the "multi-eV" axions mentioned before. Observations of three well studied clusters (Abell 1413, 2218 and 2256) at Kitt Peak National Observatory [39, 40] have seen no axion decay line, excluding the range

  $$3\,\text{eV} < m_a < 8\,\text{eV}\,.$$

  The radio telescope search, was performed under the assumption that axions dominate potential walls. Had axions been present in dwarf galaxies, they would decay

into photons that would be detected as narrow lines in radio telescope power spectra ([41]). The observations made in Haystack Observatory raise a bound on the axion-to-photon coupling at

$$g_{a\gamma} < 1.2 \times 10^{-9}\,\mathrm{GeV}$$

of axions with a mass

$$298\,\mu\mathrm{eV} \lesssim m_a \lesssim 363\,\mu\mathrm{eV}\ .$$

- **"Shining through a wall" experiments:** Given the coupling of axions to photons, one can expect axions to be created when a light beam (usually laser) travels inside a transverse magnetic field. If the exit of the laser beam is blocked (with a "wall"), only the axion beam will pass through the wall, and entering a second transverse magnetic field would be re-converted to detectable photons [42]. An experiment done using this technique ([43] and [44]), bound the coupling of axions with mass

$$m_a < 10^{-3}\,\mathrm{eV}$$

to photons to

$$g_{a\gamma} < 6.7 \times 10^{-7}\,\mathrm{GeV}^{-1}\ .$$

- **Polarization experiments:** The same experiment put limits on the axion mass and coupling to photons using the notation that axions would induce small changes in the polarization state of the photon beam that produces them, responsible for two observable effects [45]:

  Dichroism As the laser beam propagates in the magnetic field, the component of the electric field parallel to the magnetic field ($\vec{E}_{\parallel}$) will be reduced because of the production of axions, resulting in *dichroism*, a rotation of the polarization vector.

  Vacuum Birefringence In the second step, as the axion beam passed through the second magnetic field, the initially linearly polarized beam will become elliptically polarized (axions will mix again with $\vec{E}_{\parallel}$).

  They restricted [46] the axion-to-photon coupling for

$$m_a < 5 \times 10^{-4}\,\mathrm{eV}$$

to

$$g_{a\gamma} < 3.6 \times 10^{-7}\,\mathrm{GeV}^{-1}\ .$$

  A more recent experiment, PVLAS [47] started taking data in late 2002. Although their primary goal is to measure the magnetically induced birefringence and optical activity of the vacuum element, they do have the ability to produce and detect axions (or axion-like particles) within their apparatus.

- **Solar axion searches:** It has already been discussed that axions could provide an extra cooling mechanism for the stars, in the cores of which they must be produced efficiently. The closest and best known star that can be used for observation is the Sun. Using again the Primakoff process, two types of "helioscopes" have been built:

  * Axions can interact coherently in the electric field in the neighbourhood of the atomic nuclei in crystals, when the Bragg condition is fulfilled [48]. Germanium crystal detectors have been implemented for these searches, and two groups have looked for axions with this technique, SOLAX [49] and COSME [50]. The results they reached are rather similar

    $$g_{a\gamma} < 2.7 \times 10^{-9}\,\mathrm{GeV}^{-1} \;\; [SOLAX]$$

    and

    $$g_{a\gamma} < 2.8 \times 10^{-9}\,\mathrm{GeV}^{-1} \;\; [COSME]$$

    for axion masses up to $m_a \lesssim 1\,\mathrm{keV}$. The DAMA experiment is using NaI(Tl) [51] crystals and achieved a limit of

    $$g_{a\gamma} < 1.7 \times 10^{-9}\,\mathrm{GeV}^{-1} \;\; [DAMA] \;\; .$$

  * The second type of "helioscopes" make use of the conversion of axions to photons in a magnetic field; they provide the axions coming from the Sun with a magnetic field, transverse to their course, which will help them convert into a 'to-be-detected' photon. The first experiment of this type ([52]) explored two regions in the mass range :

    $$g_{a\gamma} < 3.6 \times 10^{-9}\,\mathrm{GeV}^{-1} \;\; \text{for} \;\; m_a < 0.03\,\mathrm{eV}$$

    and

    $$g_{a\gamma} < 7.7 \times 10^{-9}\,\mathrm{GeV}^{-1} \;\; \text{for} \;\; 0.03\,\mathrm{eV} < m_a < 0.11\,\mathrm{eV}\,.$$

    A more recent experiment was performed in Tokyo ([53]), having better sensitivity has given the following limits:

    $$g_{a\gamma} < 6 \times 10^{-10}\,\mathrm{GeV}^{-1} \;\; \text{for} \;\; m_a < 0.03\,\mathrm{eV}$$

    and

    $$g_{a\gamma} < 6.8 - 10.9 \times 10^{-10}\,\mathrm{GeV}^{-1} \;\; \text{for} \;\; m_a < 0.3\,\mathrm{eV}\,.$$

  The Cern Solar Axion Telescope (CAST), that will be described in detail in the following, belongs to this type of searches.

Chapter 3

The CERN Axion Solar Telescope Experiment

In this chapter the principle and the components of the CAST experiment [54] are described: the concept of the experiment is to have a magnetic field aligned with the center of the Sun for the longest time interval possible; the incoming axion will interact with the magnetic field -when the coherence condition is fulfilled- and will be converted to a photon, giving it its energy and momentum. Therefore the main components needed to perform the experiment are: the Sun, a magnet (pointing to the direction of the Sun) and photon detectors. The sensitivity of the experiment increases with the implementation of an X-ray focusing device.

3.1 The Sun as a source of Axions

Like in the case of any other star, the interior of the Sun can offer the electric fields (of nuclei and electrons "targets") in the plasma to photons that will consequently convert to axions. In the case of small momentum transfer this process is better viewed as interactions with coherent field fluctuations in the plasma [55], while for a large momentum transfer it can be viewed as the Primakoff process [56, 57] (figure 3.1):

$$\gamma + Ze \rightarrow Ze + a \quad .$$

Recoil effects of these targets can be neglected considering the rather small (few keV)

Figure 3.1: The Primakoff effect in the Sun (left) and the inverse process in the laboratory-magnet (right).

photon energies compared to the electron mass. Assuming a nonrelativistic plasma, after integrating over all possible species of targets and over all angles, the transition rate of a photon of energy w into an axion is given by

$$\begin{aligned}\Gamma_{\gamma\to a} &= \frac{g_{a\gamma}^2\, T_\odot\, \kappa_s^2}{32\pi}\,\frac{k}{w}\left\{\frac{[(k+p)^2+\kappa_s^2]\,[(k-p)^2+\kappa_s^2]}{4\,k\,p\,\kappa_s^2}\ln\left[\frac{(k+p)^2+\kappa_s^2}{(k-p)^2+\kappa_s^2}\right]\right.\\ &- \left.\frac{(k^2-p^2)^2}{4\,k\,p\,\kappa_s^2}\ln\left[\frac{(k+p)^2}{(k-p)^2}\right]-1\right\}\ , \end{aligned} \tag{3.1}$$

where k and w are the momentum and energy of the photon, p the axion momentum and $T_\odot$ the temperature of the Sun. Screening effects are described by the Debye-Hückel scale κ_s :

$$\kappa_s^2 = \frac{4\pi\alpha}{T_\odot}\sum_j Z_j^2\, N_j\ , \tag{3.2}$$

using N_j for the number density of charged particles carrying charge $Z_j e$.

The energy of the axion is practically the energy of the photon; the plasma frequency in the Sun is small (around 0.3 keV) and can be ignored (to first approximation) in comparison to the photon energies, typically $3T_\odot \approx 4\,\mathrm{keV}$ ($T_\odot \approx 1.3\,\mathrm{keV}$ in the solar center). Hence one can write $k = E_a$ and $p = \sqrt{E_a^2 - m_a^2}$, with E_a the axion energy and m_a the axion mass and change equation (3.1) into

$$\begin{aligned}\Gamma_{\gamma\to a} &= \frac{g_{a\gamma}^2\, T_\odot\, \kappa_s^2}{32\pi}\left\{\frac{(m_a^2-\kappa_s^2)^2+4\,E_a^2\,\kappa_s^2}{4\,E_a\,p\,\kappa_s^2}\ln\left[\frac{(E_a+p)^2+\kappa_s^2}{(E_a-p)^2+\kappa_s^2}\right]\right.\\ &- \left.\frac{m_a^4}{4\,E_a\,p\,\kappa_s^2}\ln\left[\frac{(E_a+p)^2}{(E_a-p)^2}\right]-1\right\}\ . \end{aligned} \tag{3.3}$$

To obtain the differential flux of axions at Earth, the transition rate is folded over the blackbody photon distribution of the Sun. Integrating over a standard solar model [58]:

$$\frac{d\Phi_a(E_a)}{dE_a} = \frac{1}{4\,\pi\,r_E^2}\int_0^{R_\odot} d^3r\,\Gamma_{\gamma\to a}\,\frac{1}{\pi^2}\,\frac{E_a^2}{e^{\,E_a/T_\odot}-1} \tag{3.4}$$

where r_E is the distance between the Sun and the Earth ($r_E = 1.50\times10^{13}\,\mathrm{cm}$) and $R_\odot$ the radius of the Sun.

In reference [56], a well approximated analytic formula for the differential axion spectrum is given :

$$\frac{d\Phi_a(E_a)}{dE_a} = 4.02\times10^{10}\left(\frac{g_{a\gamma}}{10^{-10}\mathrm{GeV}^{-1}}\right)^2\frac{(E_a/\mathrm{keV})^3}{e^{\,E_a/1.08\,\mathrm{keV}}-1} \qquad \left[\mathrm{cm}^{-2}\mathrm{s}^{-1}\mathrm{keV}^{-1}\right] \quad . \tag{3.5}$$

The spectrum is plotted in figure 3.2. The distribution shows an average energy for the axions of $< E_a >= 4.2$ keV.

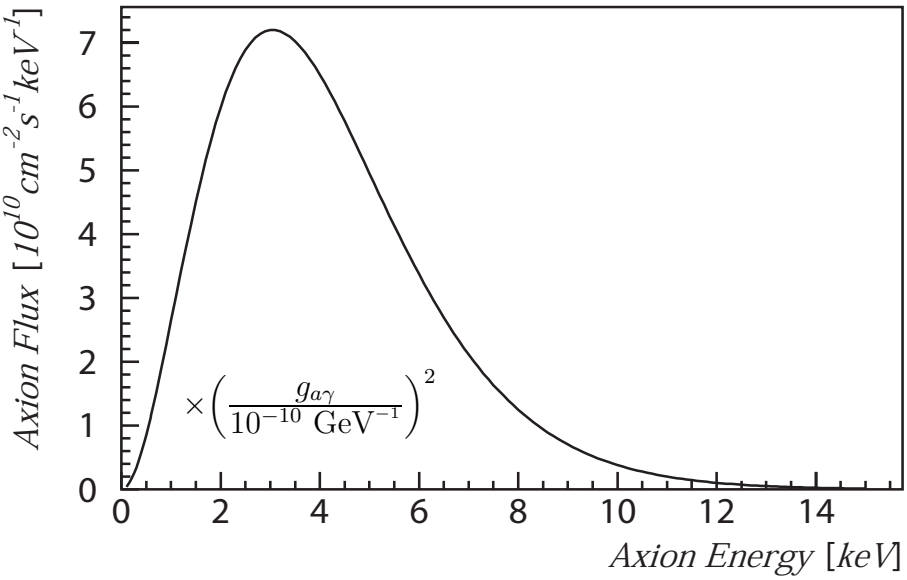

Figure 3.2: The differential solar axion flux at the Earth. The maximum appears at an energy of 3 keV, while the mean value lies at 4.2 keV [56].

Modern solar model

Following equation (3.5), the solar axion number flux at Earth –using a 1982 solar model– is found to be

$$\Phi_a = 3.54\times10^{11}\left(\frac{g_{\alpha\gamma}}{10^{-10}\,\mathrm{GeV}^{-1}}\right)^2\,\mathrm{cm}^{-2}\,\mathrm{s}^{-1}$$

A more recent calculation [59, 60], using a modern solar model gives

$$\Phi_a = 3.75 \times 10^{11} \left(\frac{g_{\alpha\gamma}}{10^{-10}\,\mathrm{GeV}^{-1}} \right)^2 \mathrm{cm}^{-2}\,\mathrm{s}^{-1}$$

and a fit function for the differential flux :

$$\frac{d\Phi_a(E_a)}{dE_a} = 6.02 \times 10^{10} \left(\frac{g_{a\gamma}}{10^{-10}\mathrm{GeV}^{-1}} \right)^2 \frac{(E_a/\mathrm{keV})^{2.481}}{e^{\,E_a/1.205\,\mathrm{keV}} - 1} \qquad \left[\mathrm{cm}^{-2}\mathrm{s}^{-1}\mathrm{keV}^{-1}\right] \quad . \tag{3.6}$$

A comparison between the two equations shows that the axion flux expected depends only slightly on the exact solar model.

3.1.1 Solar axion detection in a magnetic field

The Primakoff effect consists practically of an interaction between the axion coming from the Sun and a virtual photon provided by the magnetic field. Anyone of those virtual photons could be the one taking part in this conversion, at any length of the field for which the interference will be *constructive* (the coherence condition). The conversion process remains coherent when the axion and photon fields remain in phase over the length of the magnetic field [61]. Taking this into account, the axion-to-photon conversion probability in vacuum is calculated as

$$P_{a\to\gamma} = \left(\frac{B g_{a\gamma}}{2} \right)^2 2L^2 \frac{1 - \cos^2(qL)}{(qL)^2} \quad , \tag{3.7}$$

where B and L are the magnetic field and length. q indicates the momentum transfer between the axion and the X-ray photon:

$$q = \frac{m_a^2}{2\,E_a} \quad . \tag{3.8}$$

The coherence condition then is satisfied for

$$qL < \pi \quad . \tag{3.9}$$

For a 10 m long magnet and the expected energy spectrum (with a mean energy of $\sim 5\,\mathrm{keV}$), this condition brings the limit on the mass up to which such an experiment is sensitive in vacuum to $m_a < 0.03\,\mathrm{eV}$.

However, using an X-ray absorbing buffer gas, the transition rate $P_{a\to\gamma}$ changes according to equation (3.10), where the absorption in the gas is taken into account.

$$P_{a\to\gamma} = \left(\frac{B g_{a\gamma}}{2} \right)^2 \frac{1}{q^2 + \Gamma^2/4} \left[1 + e^{-\Gamma\,L} - 2e^{-\Gamma\,L/2} \cos(qL) \right] \quad , \tag{3.10}$$

with Γ the inverse photon absorption length for the X-rays in the medium. In this case, the momentum transfer q becomes

$$q = \left| \frac{m_\gamma^2 - m_a^2}{2E_a} \right| \ , \tag{3.11}$$

for m_γ the photon effective mass (given by the plasma frequency) in the buffer gas

$$m_\gamma \simeq \sqrt{\frac{4\pi n_e}{m_e}} = 28.9\sqrt{\frac{Z}{A}\rho} \ , \tag{3.12}$$

where n_e is the number density of electrons, m_e the electron mass, and the dependence on the atomic number Z and mass A as well as the gas pressure P are evident. In the case of hydrogen or helium (at 300 K), one can calculate $m_\gamma = \sqrt{P[\text{atm}]/15}$. Now the coherence is restored for a narrow mass window, for which the "mass" of the photon matches that of the axion such that

$$qL < \pi \quad \Longrightarrow \quad \sqrt{m_\gamma^2 - \frac{2\pi E_a}{L}} < m_a < \sqrt{m_\gamma^2 + \frac{2\pi E_a}{L}} \ , \tag{3.13}$$

which brings the sensitivity of the mentioned experiment with a helium buffer gas at 1 atm[1] up to an axion mass of 0.3 eV. Figure 3.3 shows an example of two measurements, one in vacuum and one in 6.08 mbar .

Of most interest is the number of photons N_γ expected after the conversion

$$N_\gamma = \int \frac{d\Phi_a(E_a)}{dE_a} \, S \, t \, P_{a\to\gamma} \, dE_a \ , \tag{3.14}$$

where S is the effective area of the detector, and t the measurement time in days. Equation (3.14) exhibits the importance of the measurement's time, and does not include the factor of the detector's efficiency.

The agenda of the CAST experiment included the exploitation of every possibility to cover the wider range of potential axion masses, and foresaw two phases:

Phase I covers the conversion of axions-to-photons in vacuum. For the parameters of CAST (see below details on B an L), equation (3.9) gives as an upper limit of sensitivity a mass of 0.02 eV.

Phase II supposes filling the magnet pipes with a gas. Thus the sensitivity restriction to 0.02 eV, that the coherence condition imposed for vacuum, is lifted. During this phase the sensitivity of the experiment will be extended up to 0.82 eV (see last chapter).

The predicted sensitivity of the CAST Experiment for both Phase I and Phase II is shown in figure 7.1.

[1]Most of the times the temperature of operation is 1.8 K. The 1 atm of the 300 K is translated to 6.08 mbar in 1.8 K .

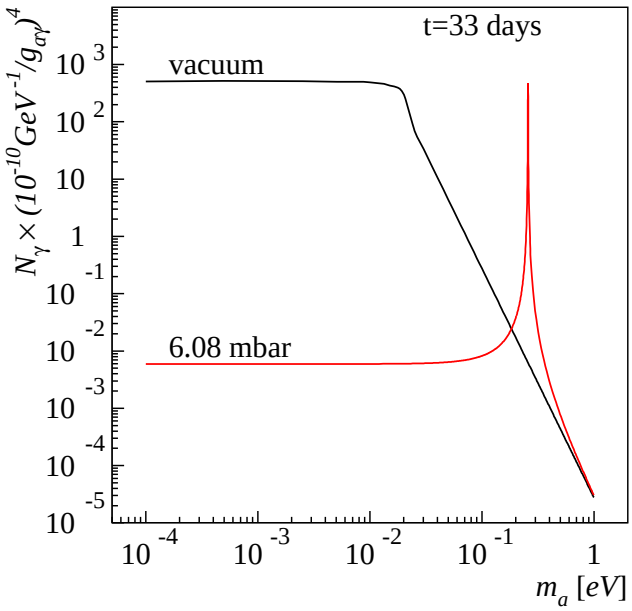

Figure 3.3: A comparison between measuring in vacuum and in the presence of a gas. In the case of the vacuum (black line), when reaching a certain mass the transition rate is no longer maximum, but decreases rapidly. The presence of the gas, helps restore this transition rate to its maximum for a very narrow mass window, producing the narrow peak in the plot (red line).[The number of photons has been calculated supposing data for 33 days for each of the two measurements, and a coupling constant of 1×10^{-10} GeV^{-1}.]

3.2 The Experiment

The magnet

The first prototype superconducting magnets built for the Large Hadron Collider (LHC) were considered ideal to play the host for the axion to photon conversion (figure 3.4). They are twin-aperture (43 mm in diameter) and can provide a magnetic field of a 9 T intensity over the 9.26 m long straight beam pipes [62] (figure 3.5).

To reach the field of 9 T (corresponding to 13300A), the magnet has to be operated in superfluid helium in a temperature of 1.8 K. A whole cryogenic plant needed to support and maintain the operation of the magnet (figure 3.6) was set up by recovering and adapting parts from the dismounted e^+e^- LEP collider and DELPHI, as well as a newly purchased Roots pumping group, responsible for the final stage of cooldown and operation. The cryogenic and electrical feed is done through the Magnet Feed Box (MFB), connected to one end of the magnet, while a Magnet Return Box (MRB) closes the opposite end. Figure 3.7 shows the modified flow scheme of the MFB with its interface of 7 flexible transfer lines that connect to the liquid helium supply, gaseous helium pumping group

Figure 3.4: A picture of the CERN Axion Solar Telescope in the experimental Hall. The 10 m long magnet is moving with the help of a platform sitting on two ends: a turntable on the right, allowing it to move ±40° horizontally, and a girder (left) supporting the two screws that move the magnet ±8° vertically. The turntable holds the weight of the MFB, while the much less weight of the MRB is born by the screws. The flexible helium transfer lines were designed to allow the movement of the magnet without interrupting its cryogenic operation.

and quench recovery system.

Fluctuations on parts of the cold mass might increase the temperature locally and turn the helium non superconducting. The detection of a resistive transition of the magnet at nominal current triggers a "quench". The results of a quench are rapid increase of pressure and helium discharges from the cryogenic system even to the atmosphere, if the pressure in the helium recovery collector exceeds some limits. A quench protection system monitors several signals that can prove harmful for the system, and triggers a quench to protect the cryoplant when necessary. The re-start of the automatic cooldown of the cold mass to 1.8 K (which was warmed up to 40 K as a result of the dumped energy) requires a manual acknowledge by the operator and takes approximately 6-8 hours[2].

Platform and motors

With a view to maximizing the time the magnet is aligned with the Sun (and therefore the data taking time), a platform (girder) was built that would allow for the magnet to

[2]As it will be mentioned later, several false signals picked up from this system were to blame for a big number of "fake" quenches during 2003, which interrupted the data taking of the experiment.

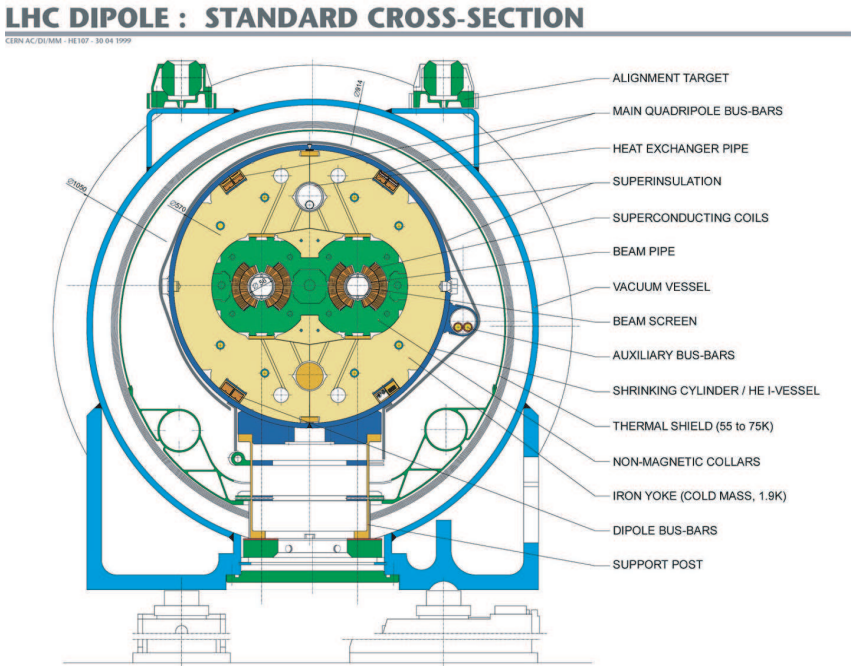

Figure 3.5: The cross section of the straight-bore, twin-aperture LHC dipole prototype [CERN].

point at the Sun's core for the longest period possible.

The platform (figure 3.4) consists of two metallic supports; one of them is responsible for the guiding of the platform and moves on special rails at an angle of approximately 80° in the azimuthal direction, while at the same time carries two screws that are responsible for its vertical movement. The other support carries the most of the weight (one has to take into account that the weight of the complex magnet-cryogenics is close to 40 tons) and rotates around the horizontal. Because of mechanical constraints imposed by the magnet manufacturers[3], the vertical movement of the platform is constrained to ±8°, which allows that the magnet can be aligned with the Sun for approximately 3 hours every day (∼ 1.5 h during sunrise and the same time during sunset). Including the horizontal range of movement, the total amount of time that the magnet is aligned to the core of the Sun is approximately 50 days over one year.

Two motors, accompanied by two encoders, are assigned with the moving of the platform, each dedicated to one direction. This motorized system is taking orders from a rather sophisticated software program, responsible for directing the magnet to the Sun –and moving the magnet in general.

[3]The cryostat sits inside a metallic vessel (in colour blue in picture (3.4)) to which it is connected via thermally isolating feet. The mechanical strains in these feet put a limit to the maximum allowed inclination of the cryostat.

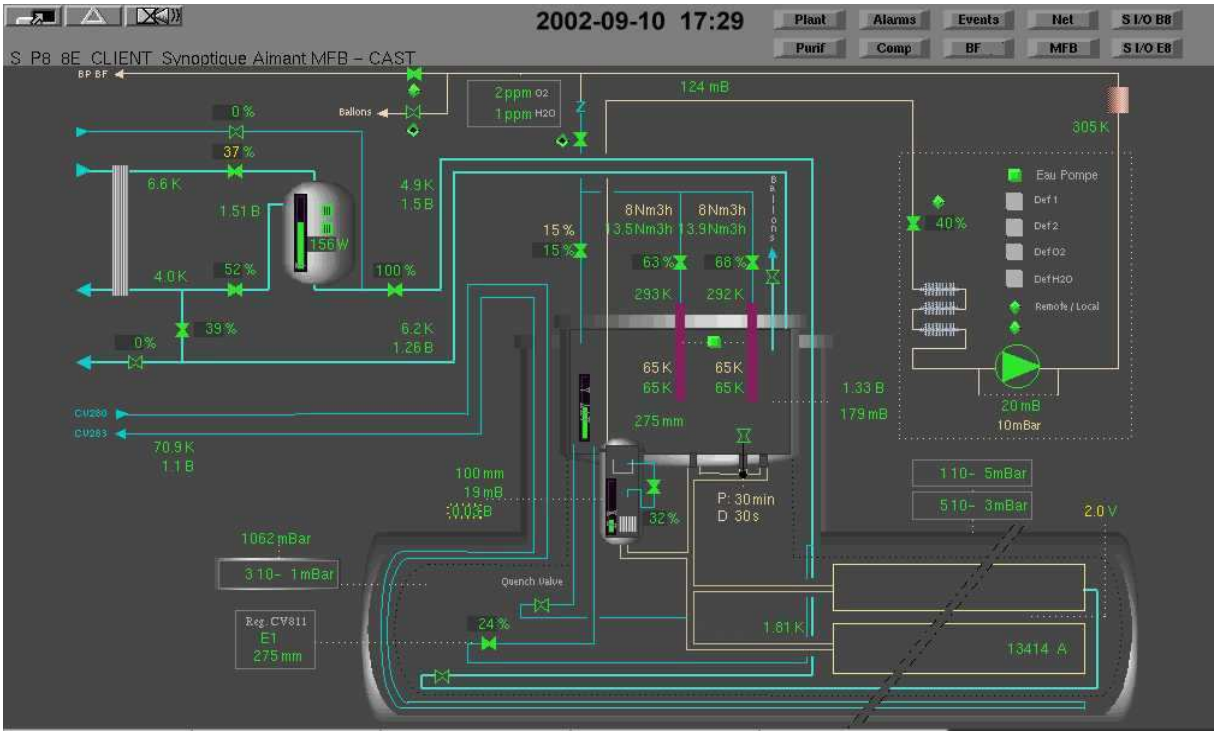

Figure 3.6: The process control mimic of the cryogenic system in CAST: valves' condition, helium flows, cooling and purification system at a glance [63] .

The tracking software

The logic of this program's work is shown schematically in figure 3.8. The software (written in LabView) calls an executable file based on NOVAS (Naval Observatory Vector Astrometry Subroutines) [64], which in turn reads the time and date of the PC and calculates the solar azimuthal angle and zenith distances (AZ, ZD), for the telescope's coordinates[4], for the next minute. With these points given, it finds the corresponding encoder values, looking up the tables $V_x(AZ, ZD)$ and $V_y(AZ, ZD)$, and directs the motors to that position.

Given their importance, these tables were constructed with the maximum possible accuracy. With the help of the surveyors of the EST division at CERN, a large number (90) of magnet positions (AZ, ZD) was mapped down in encoder values, forming tables $V_x(AZ, ZD), V_y(AZ, ZD)$ with an accuracy of 0.001°. Using the spline interpolation method ("Hardy's multiquadratic") for filling in the gaps that the real (and finite) measurements left, the precision is always better than 0.01° (typically around 0.002°).

Of similar importance is the continuous check –and correction, when needed– of the hosting PC's clock. The system is checking the time with two CERN time servers, and is running an NTP demon which produces a continuous time synchronization to the order of 1ms. It should be mentioned that the Daylight Savings Time (DST) changes are taken

[4]In practice CERN coordinates, 46°15′N, 6°5′E, 330 m above sea level.

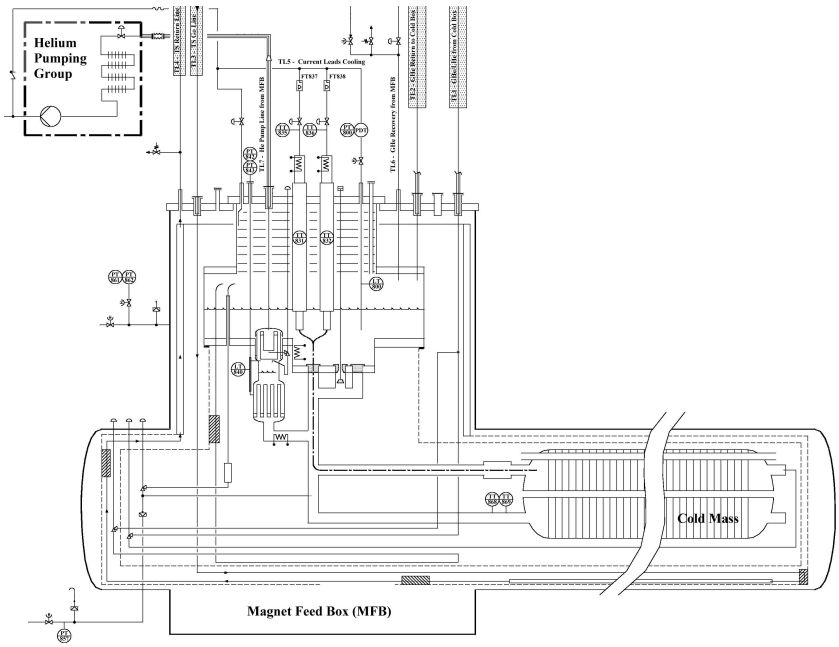

Figure 3.7: The flow scheme of the Magnet Feed Box (MFB) for the CAST experiment (taken from [63]).

into account in the executable .

Trying to sum up all possible error sources and their estimated values, Table 3.1 is formed.

The table shows that the estimated precision is very good indeed for CAST. And yet, an image would be more eloquent. Despite the difficulties imposed by the location of the telescope, optical verification of this precision is possible; an optical telescope is aligned with the magnet axis and is coupled to a CCD camera. Twice a year, in mid-March and mid-September, when the Sun passes by a window specially made for this purpose and assuming that the weather permits it, the tracking software[5] points the magnet to the Sun, and the camera films during the movement. A close examination of the frames afterwards leads to a conclusion on the precision of the tracking (figure 3.9).

Apart from moving the magnet, the tracking software logs useful information like the temperature in the experimental hall, the ambient pressure, the value of the intensity of the field inside the magnet. During the second year of operation, the recording of more information was needed, therefore an independent slow control acquisition was used.

[5]In fact it is a second version of the tracking software, in which the refraction of light in the atmosphere is corrected for.

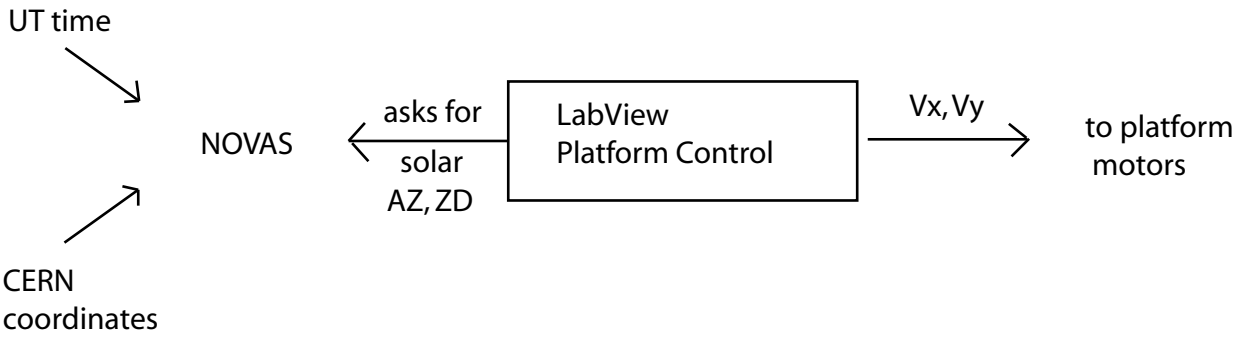

Figure 3.8: The scheme of the operation principle of the tracking program.

Table 3.1: Possible sources of errors on the precision of the magnet's position when following the Sun

Error source	**Typical value**	**Maximum value**
Astronomical Calculations	0.002°	0.006°
Grid Measurements (precision of 0.2mm)	0.001°	
Uncertainty of CERN coordinates	∼0.001°	
Interpolation of grid measurements	0.002°	<0.01°
Horizontal encoder precision	∼0.0014°	
Vertical encoder precision	∼0.0003°	
Perfect linearity of motor speeds	<0.002°	
Clock time	∼0°	
TOTAL	<0.01°	

Slow Control

The slow control started (in late July 2003) recording information useful for the monitoring of the system, as well as information that proves very useful in the analysis of the data acquired. More specifically, it is a LabView application checking and logging information like

- the pressure and temperature inside the cryostat and in front of each detector,
- the load each of the two lifting screws is carrying,
- the position of the magnet in motor encoder values and in angles taken from an independent positioning system,
- the condition of the magnet valves (open or closed),
- the permission (or lack of it) to open a valve,
- indication of alarms regarding the system.

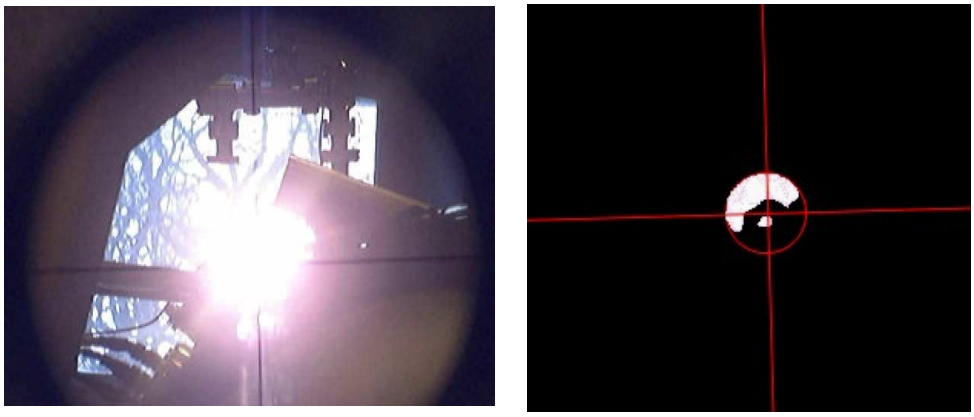

Figure 3.9: The filming of the Sun: an optical verification that the software is really pointing the magnet to the center of the Sun, can be performed twice a year. On the left can be seen one frame taken while tracking, and on the right a superposition of many frames (taken with filters). The cross indicated the center of the Sun as we follow it, which is in good agreement with the image.

The alarm system was established with the help of several interlocks (on a fail-safe mode), regarding the condition of elements that are vital for the operation, like the handling of the valves according to the vacuum level in front of the detectors, the check on the compressed air supply from the network, a quench signal, a power failure, flammable gas supply.

3.3 The detectors

With a powerful magnet ready to follow the Sun with great precision and convert the axions into photons, the next step is the commissioning of X-ray detectors, sensitive to the $1-10\,\mathrm{keV}$ range. Two of the bores of the magnet, looking for "sunset" axions, are covered by a conventional TPC chamber. On the opposite side, on one bore a MICROMEGAS detector is waiting, and next to it an X-ray mirror telescope focuses the photons coming from the last free bore onto a CCD.

3.3.1 The X-ray focusing device

The X-ray mirror telescope would produce an "axion image" of the Sun, by focusing the photons from axion conversion in the magnetic field onto an X-ray CCD (figure 3.10).

This focusing of photons from an area of approximately $15\,\mathrm{cm}^2$ to an image of $7\,\mathrm{mm}^2$ (a compression factor of 200), improves the signal to noise ratio by two orders of magnitude, without taking into account that the system's transmission is of the order of 35%. The other advantage is the measuring of signal and background at the same time, reducing any systematic effects.

The Wolter I type X-ray mirror telescope of CAST is a prototype of the German X-ray satellite mission ABRIXAS [65, 66]. It consists of a combination of 27 nested, gold coated parabolic and hyperbolic mirror shells with a focal length of 1600 mm. The maximum diameter of the outer mirror shell is 163 mm while the smallest shell has a diameter of 76 mm. A spider-like structure supports the individual mirror shells on their front side and divides the aperture of the telescope in six sectors. Given that the diameter of the CAST magnet bore is 43 mm, only a fraction of the full aperture of the telescope is used; only one of the six mirror sectors is illuminated by the nearly parallel X-ray beam coming from the magnet (axions converted into photons), as the telescope is mounted on the magnet non-centrically.

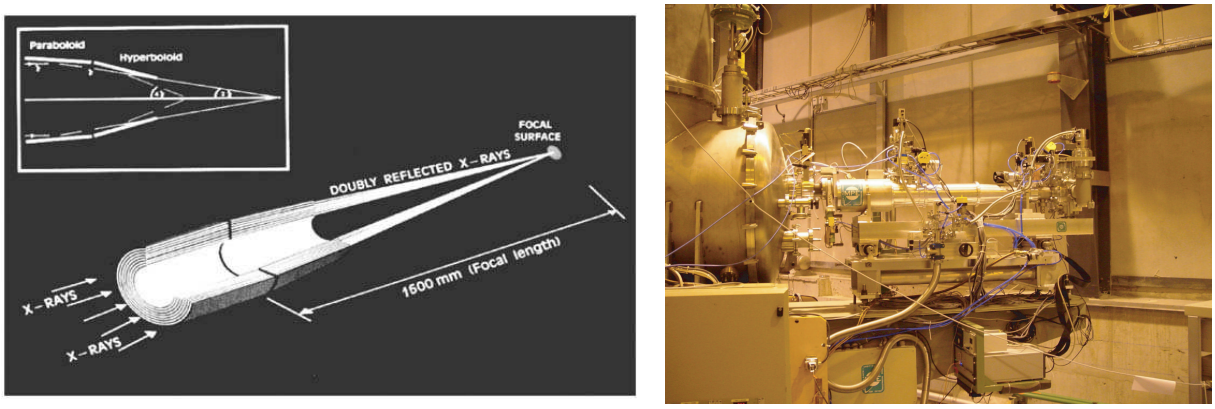

Figure 3.10: Left: The principle of the Wolter I type telescopes. The X-ray photons are reflected twice by a combination of parabolic and hyperbolic mirror surfaces. Reflection is achieved at very shallow angles, on mirrors with a surface roughness of only a few nm. Right: A picture of the X-ray telescope of CAST (X-ray focusing device - pnCCD) as installed in the CAST experiment.

Any contamination and adsorption on the mirror reflective surface, would result in a degradation of the efficiency, therefore the whole system is operated under vacuum conditions (below 10^{-5} mbar).

The pn-CCD detector, on which the X-rays are focused, is a prototype developed for the European XMM-Newton X-ray observatory, and its operation principle along with its performance are described in detail in [68] and the references therein. A thin (20 nm) uniform radiation entrance window enables the detector to reach an efficiency of almost 100% over the range of interest, since it can work in vacuum directly connected to the magnet vessel, without the need of any additional window.

The CCD chip has a set of 200×64 pixels, each of a size of $150 \times 150\,\mu\text{m}^2$. Therefore its sensitive area ($1 \times 3\,\text{cm}^2$) is larger than the expected image of the inner part of the Sun ($0.2R_\odot$) , which would have a diameter of 2.83 mm (19 pixels). Exactly this feature consists the major advantage of the whole telescope-CCD system; it enables the simultaneous measuring of the potential axion signal (expected inside the "spot") and the background (the rest of the detector's sensitive area), allowing a reduction on the systematic errors in

background subtraction, and eliminating uncertainties due to time or position variation.

To improve the background, shielding was installed both inside and outside the detector's vessel (figure 3.11). A combination of copper and lead on the inside and an additional wall of lead enclosing the whole vessel, reduces the background from external sources (cosmic rays, gamma rays).

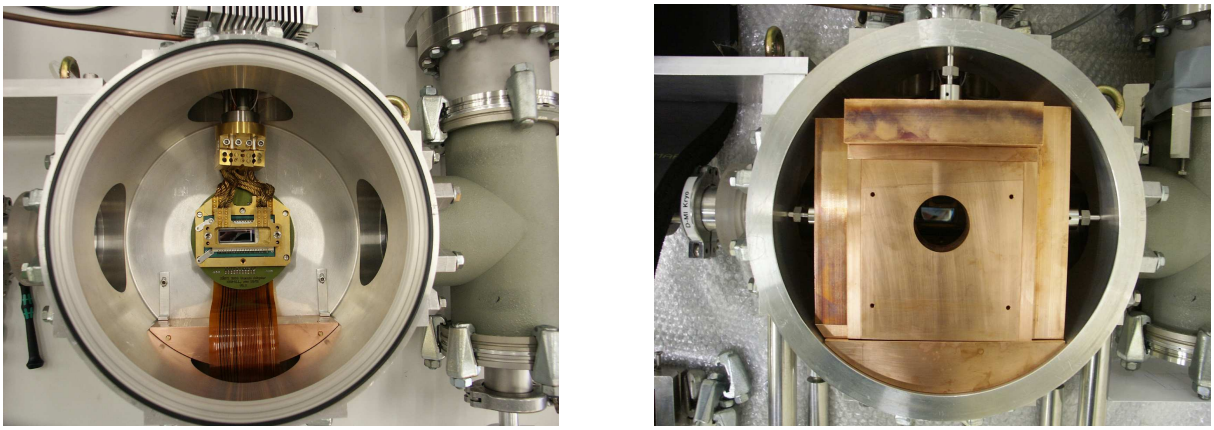

Figure 3.11: Left: The front view of the pn-CCD detector vessel, showing the pn-CCD chip (center) and vacuum components (right side of the image). Right: The detector with the inner shielding components. The shield consists of (from outer to inner parts): a 2 cm thick layer of low activity copper and a 2.2 cm thick layer of low activity, ancient lead encapsulated in copper. An additional 2.5 cm lead shield is installed outside the detector's vacuum housing.

3.3.2 The Time Projection Chamber

The CAST Time Projection Chamber (TPC) is a robust design, following the well-known concept of a conventional TPC (figure 3.12, left): a large gaseous volume in which the primary interaction takes place, producing ionization electrons that drift towards a plane of wires where, as in a MWPC, the avalanche process that produces the amplification of the signal is developed.

It has a conversion volume of $10 \times 15 \times 30\,\mathrm{cm}^3$. The 10 cm drift direction is parallel to the magnet beam axis, and the section of $15 \times 30\,\mathrm{cm}^2$ is perpendicular to that direction, covering both magnet bores (which each have a diameter of 42 mm and their centers are separated by 18 cm). The volume is filled with gas Ar(95%)/CH_4(5%) at atmospheric pressure and allows for essentially total conversion (>99%) of photons up to 6 keV crossing the chamber parallel to the magnet beam direction. The conversion efficiency decreases for higher energies.

An aluminum layer located on the inner side of the chamber wall closer to the magnet acts as the drift electrode. The drift electrode is kept at $-7\,\mathrm{kV}$ in order to produce a field of $700\,\mathrm{kV/cm}$ (figure 3.12). On the back side of the chamber, the wires are arranged in

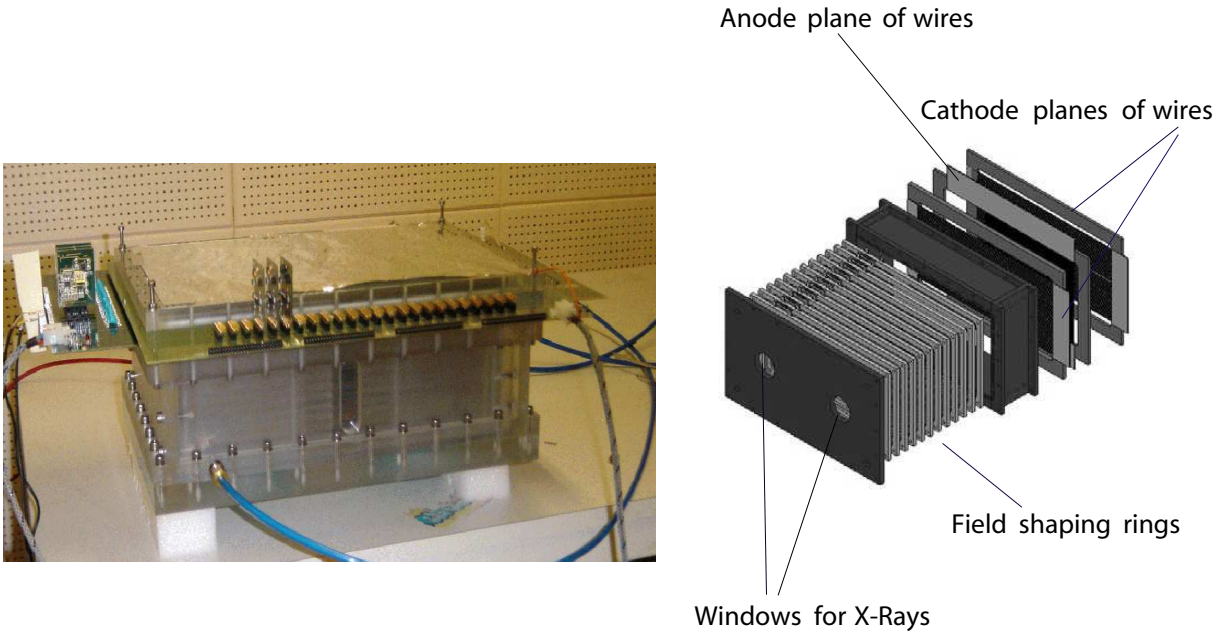

Figure 3.12: Left: A picture of the detector volume. Right: An exploded view of the detector showing all its parts.

3 planes, one anode plane at +1.8 kV between two grounded cathode planes. The anode plane contains 48 wires of 20 μm diameter (gold plated tungsten), parallel to the wider side of the chamber. Each cathode plane contains 96 wires of 100 μm diameter, perpendicular to the anode wires. The distance between wires of the same plane is 3 mm. The distance between the anode and the cathode plane closest to the drift region is 3 mm, while the distance between the anodes and the outer cathode plane is 6 mm. The avalanche process occurs around the anode plane, due to the intense electric field, drawing the electrons while the ions are gathered by the cathode planes, providing with the two-dimensional position information of the event.

Because of its low natural radioactivity, plexiglass was used to build the whole chamber (apart from the wires, the PCB board holding the wires and the screws that hold the chamber together). The thickness of the plexiglass is about 2 cm, except in three places (two on the back side and one on a lateral side) where the only separation between the inner gas and the atmosphere is a thin mylar foil to allow the calibration of the chamber with low energy X-ray sources.

The detector is adjusted to the two magnet bores with the help of two very thin, alluminized (it serves as part of the drift electrode), mylar windows (3 or 5 μm) stretched on a metallic strongback on the side facing the magnet, in order to stand the pressure difference between the detector volume and the magnet vacuum.

To reduce the background of the TPC, a shielding out of copper, lead, cadmium and polyethylene was designed. Figure 3.13 shows a picture of the detector connected to the magnet, with part of the shielding mounted.

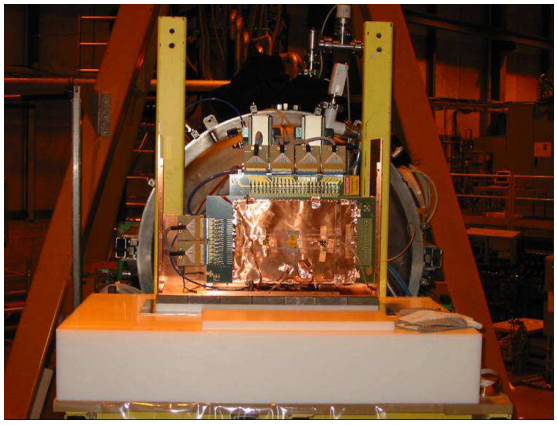

Figure 3.13: A picture of the TPC detector on the magnet; part of the shielding is built, allowing to see the copper box in which the detector is enclosed, the polyethylene wall, and in between the lead bricks.

3.3.3 MICROMEGAS

The fourth bore left, is covered by a MICROMEGAS detector (figure 3.14), which is going to be described in detail in the next chapters.

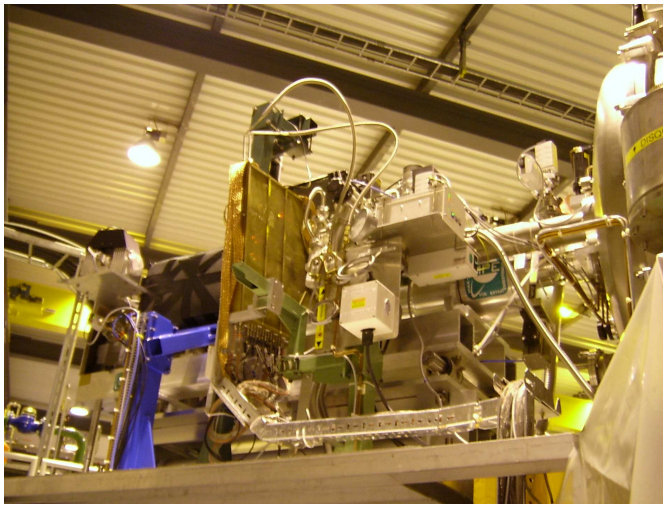

Figure 3.14: A picture of the side of the CAST magnet were the MICROMEGAS detector is attached.

3.4 Collateral

In addition to the three X-ray detectors already mentioned, a high-energy calorimeter was installed in 2004, dedicated to a parasitic search for cosmological, higher-energy axion-like particles. The high energy calorimeter will be sensitive to axion-induced gammas in the range of $\sim 100\,\mathrm{keV}$ to $\sim 150\,\mathrm{MeV}$.

Axions could be produced in the Sun, through M1 transitions (magnetic transitions), for example [69]

$$p + d \rightarrow {}^3\mathrm{He} + a \rightarrow \gamma(5.5\,\mathrm{MeV}) \quad .$$

It has been pointed out that there are more reactions in the Sun where the photon could be replaced by an axion, like the deexcitation of ^{7}Li [70] after its production by

$$\begin{aligned} {}^7\mathrm{Be} + e^- &\rightarrow {}^7\mathrm{Li}^* + \nu_e \\ {}^7\mathrm{Li}^* &\rightarrow {}^7\mathrm{Li} + a(478\,\mathrm{keV}) \quad . \end{aligned} \tag{3.15}$$

or in

$$e^+ + e^- \rightarrow \gamma + a \quad .$$

In this case, an excess signal of 511 keV would be expected when the detector is aligned with the Sun, the absence of which will impose tight restrictions on the properties of axions, maybe tighter than accelerator experiments [71].

The detector is a $0.64\,\mathrm{g}\,\mathrm{CdWO_4}$ (CWO), with the dimension $\emptyset 45\,\mathrm{mm} \times 45\,\mathrm{mm}$. Low-background techniques were implemented in the design (ancient lead for the shielding, photomultiplier with low ^{40}K content in the glass, radon displacement by flushing N_2) and for the data treatment a powerful pulse shape discrimination system was developed, able to separate internal alpha decays, spurius PMT pulses and cosmic neutron events, from γ-induced events (figure 3.15).

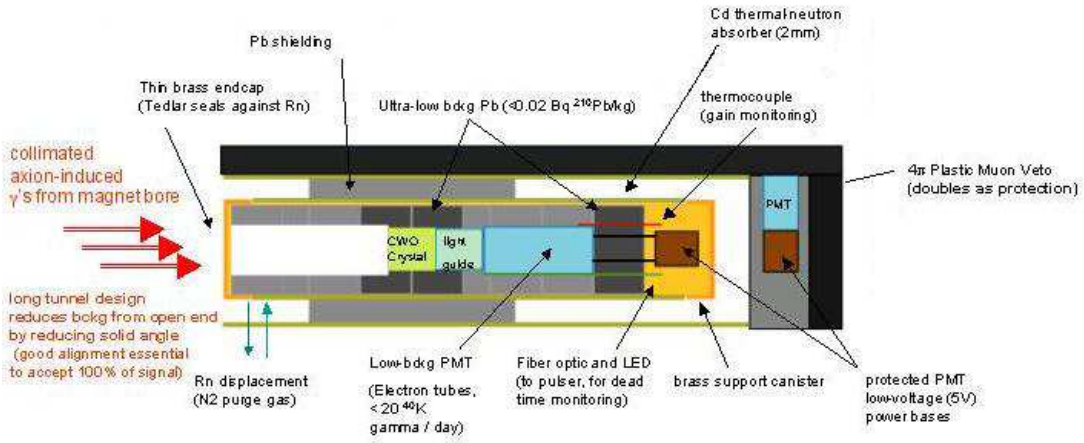

Figure 3.15: A scheme of the design of the High Energy Calorimeter at CAST.